Journal of
Materials Chemistry A

Materials for energy and sustainability

rsc.li/materials-a

ROYAL SOCIETY
OF CHEMISTRY
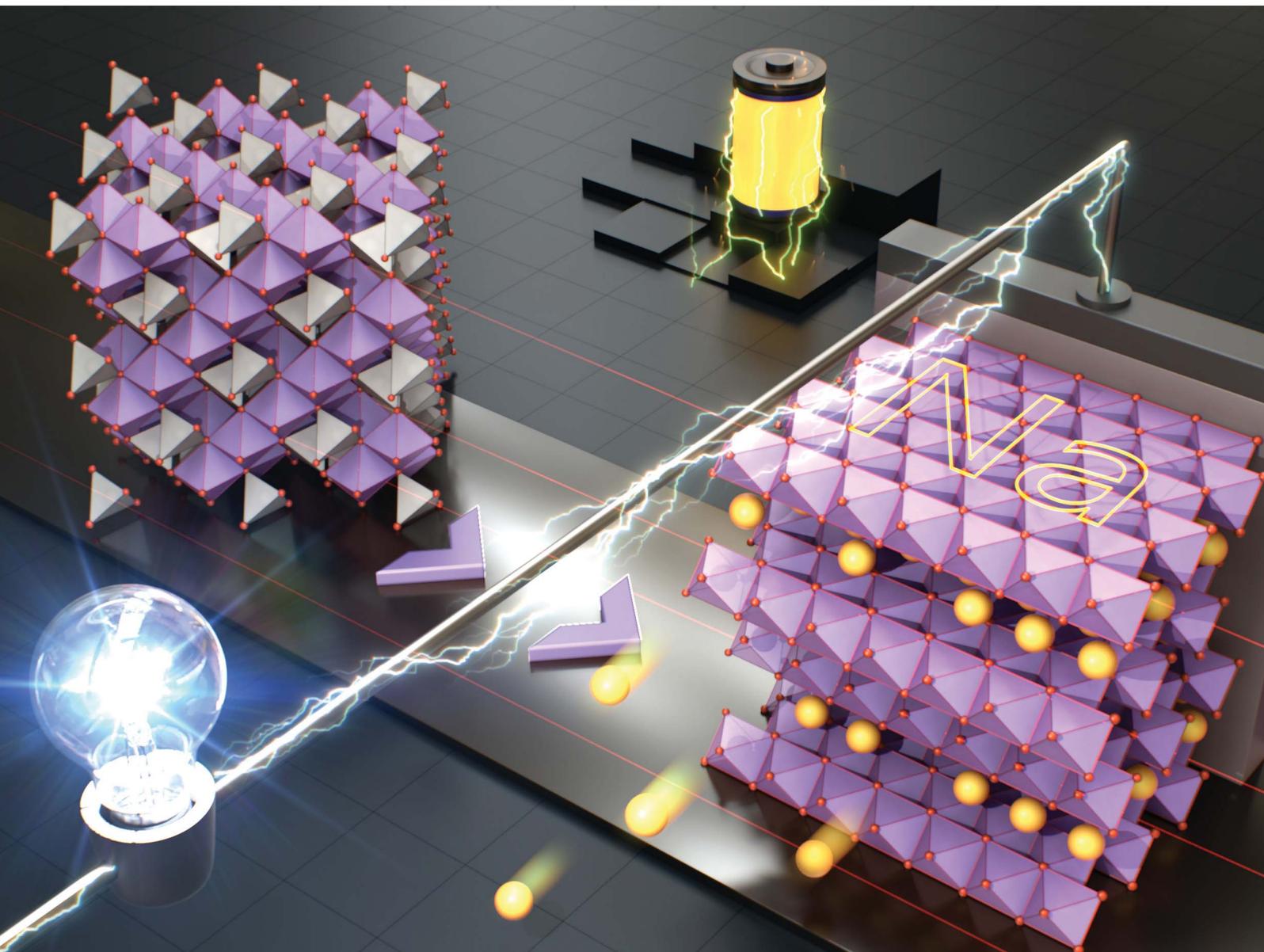
PAPER
Changhee Lee *et al.*
Designing high-performance P3-type Na$_{2/3}$[Ni$_{1/3}$Mn$_{2/3}$]O$_2$ cathodes for Na-ion batteries

ROYAL SOCIETY
OF CHEMISTRY

PAPER

Check for updates

Designing high-performance P3-type Na$_{2/3}$[Ni$_{1/3}$Mn$_{2/3}$]O$_2$ cathodes for Na-ion batteries

Changhee Lee, [ID] Shun Nakajima, Shinichi Kumakura, [ID] Tomooki Hosaka, [ID] Eun Jeong Kim [ID] and Shinichi Komaba [ID] *

P3-type layered oxide materials, where Na$^+$ ions occupy prismatic sites and layers stack in an ABBCCA sequence, have received relatively limited attention as positive electrode materials for Na-ion batteries (NIBs) due to their low temperature synthesis and poor structural stability. Unlike widely studied O3- and P2-type analogues, conventional P3-type materials often suffer from low crystallinity and mechanical fragility, leading to rapid degradation upon cycling in a non-aqueous Na cell. In this study, we report successful design of high-performance P3-type Na$_{2/3}$Ni$_{1/3}$Mn$_{2/3}$O$_2$ positive electrode materials synthesized *via* a novel pathway using spinel-type NiMn$_2$O$_4$ precursors. The resulting P3-phase exhibits distinct physicochemical features, including high crystallinity, large particle size, dispersed NiO buffer domains within the bulk, unique axis ordering, and surface exposure of {100} facets, as well as unintended compositional shifts. These attributes effectively suppress phase transitions, surface side reactions, and particle cracking, enabling superior electrochemical performances such as cycling stability and rate capability in Na cells, even without any modifications including elemental doping and surface coating. Our findings highlight the practical potential of P3-type materials through tailored synthesis, addressing key limitations and expanding the design space for next-generation NIB positive electrodes.

1 Introduction

The increasing demand for sustainable energy solutions has placed rechargeable batteries, particularly lithium-ion batteries (LIBs), at the forefront of energy storage technologies. However, challenges such as the rising cost of lithium, its limited availability, and geopolitical concerns over resource distribution have driven interest in next-generation rechargeable batteries. Among them, sodium-ion batteries (NIBs) are expected to alleviate potential supply shortages and cost pressures associated with LIBs because of large reserves with a wide geographic distribution and low cost of sodium. Furthermore, sodium, the second-lightest and second-smallest alkali metal after lithium, shares similar chemical properties with lithium, which allows NIBs to achieve relatively high electrochemical performance including energy density while benefiting from existing LIB manufacturing processes. Given these advantages, NIBs are increasingly recognized as a promising next-generation energy storage solution alongside LIBs.[1-7]

Research on positive electrode oxide materials for NIBs dates back to the 1980s when Delmas *et al.* first introduced the Na$_x$CoO$_2$ electrode.[8,9] Since then, extensive efforts have been dedicated to developing layered oxide positive electrodes, with a primary focus on O3- and P2-type structures. In these

materials, Na$^+$ ions occupy different coordination environments—typically octahedral (O) or prismatic (P) sites—depending on the polytype, which is defined based on the stacking sequence of close-packed oxygen layers. According to Delmas *et al.*, these polytypes include O2 (ABAB stacking), O3 (ABCABC stacking), P2 (ABBA stacking), and P3 (ABBCCA stacking). Generally, Na$_x$TMO$_2$ (TM: transition metal) forms an O3-type structure at high Na content ($x \sim 0.9$–1.0), while P2-type structures emerge at relatively low Na concentrations ($x = 0.6$–0.8).[10-12] Although each structure has its own advantages, both suffer from inherent limitations. For instance, while the O3-type structure offers a high initial coulombic efficiency owing to its high Na content, it undergoes a phase transition to P3 during charging through TMO$_2$ slab gliding. These structural features lead to large voltage hysteresis, significant volume change, and capacity degradation. Meanwhile, P2-type structures provide a more open framework that lowers the diffusion barrier and enhances rate capability, whereas they also suffer from a phase transition to O2-type stacking at high states of charge, leading to similar challenges such as the O3-to-P3 transition, and exhibit a lower initial coulombic efficiency due to its low Na content.[10-12]

On the other hand, the P3-type phase has received the least attention among these layered structures, primarily due to its low temperature synthesis, which is closely related to the structural/mechanical characteristics. Since Na-deficient P3-type Na$_x$CoO$_2$ ($0.5 \leq x < 1$) has been first reported,[9] which was

Department of Applied Chemistry, Tokyo University of Science, Shinjuku, Tokyo 162-8601, Japan. E-mail: komaba@rs.tus.ac.jp

prepared through solid-state reaction methods, other compositions, such as $Na_xNi_{0.22}Co_{0.11}Mn_{0.66}O_2$,[13] $Na_{0.63}Ti_{0.37}Cr_{0.63}O_2$,[14] $Na_{0.5}[Ni_{0.216}Mn_{0.784}]O_2$,[15] and $Na_{2/3}Mg_{1/3}Mn_{2/3}O_2$,[16] have been developed, demonstrating high initial capacities. Our group also reported P3-type $Na_{0.76}Ni_{0.38}Mn_{0.62}O_2$ with superior rate capability, which is attributed to a low diffusion barrier of prismatic Na^+ sites sharing a face with the TMO_6 octahedron at one side and sharing edges with the TMO_6 octahedron at another side.[17] However, these materials also undergo irreversible phase transitions to the O3 phase at high desodiation levels, which further impairs Na^+ transport kinetics and cycling performance. Another critical challenge associated with P3-type materials lies in their synthesis conditions. Unlike P2- and O3-type materials, which are typically synthesized at temperatures exceeding 850 °C, P3-type materials can be produced at relatively lower temperatures (below 750 °C). While this lower synthesis temperature can contribute to cost-effective manufacturing, it results in poor crystallinity and weak mechanical properties, leading to further rapid structural degradation caused by particle crack and easy crystallinity collapse during cycling.[18–22] Due to these limitations, P3-type positive electrode materials have been generally considered unsuitable for practical NIB applications.

In this context, this study reports the successful design and synthesis of high-performance P3-type $Na_{2/3}Ni_{1/3}Mn_{2/3}O_2$ (P3-NiMn) positive electrode materials for NIBs *via* a novel synthetic approach. In contrast to P2-NiMn, which has attracted significant attention for its outstanding properties such as superior structural stability and high reversibility in the specific voltage ranges (*e.g.*, 2.0–4.1 V (*vs.* Na)),[23] studies on P3-NiMn have remained extremely limited since its synthesis and structural properties were first reported by Dahn *et al.* in 2000 (ref. 24) and its electrochemical performance was later investigated by Kang *et al.* in 2017.[25] To address this research gap and overcome the aforementioned inherent limitations of conventional P3-type materials, we developed a unique synthesis route tailored for P3-NiMn in this study. Of special interest is that the physicochemical and electrochemical properties of the resulting P3-NiMn are thoroughly altered, compared to those of a conventionally prepared P3-NiMn obtained *via* one-step solid-state calcination using mixtures of individual transition metal and sodium sources, even without any modifications such as the doping of heteroatoms and surface coating. Based on the results, this synthetic approach is expected to significantly advance the applicability of P3-type materials as viable positive electrodes for NIBs.

2 Experimental

2.1 Material synthesis

Initially, spinel-type $NiMn_2O_4$ was synthesized *via* ball-milling and spray drying techniques to serve as a precursor for P3-NiMn. Notably, the use of $NiMn_2O_4$ as a precursor constitutes a novel synthetic route for P3-NiMn. For the spray drying method, 0.5 mol L^{-1} aqueous solutions of nickel acetate and manganese acetate (both from Fujifilm Wako Pure Chemical) were prepared, along with a 0.6 mol L^{-1} solution of citric acid

(Fujifilm Wako Pure Chemical). These solutions were mixed at a volume ratio of 5 : 1, with the molar ratio of nickel to manganese adjusted to 1 : 2. The resulting mixture was fed into a spray dryer (Mini Spray Dryer S-300, Buchi) under the following conditions: air flow rate of 20 m^3 h^{-1}, inlet temperature of 200 °C, atomizing pressure of 1000 L h^{-1}, and a feed rate of 5 mL min^{-1}. The collected powder was subsequently calcined in air at various temperatures for 3 hours to obtain $NiMn_2O_4$. To synthesize P3-NiMn, the as-prepared $NiMn_2O_4$ was mixed with sodium carbonate (Nakarai Tesque) in stoichiometric proportions and calcined in air at 625 °C for 15 hours. The sample was then quenched to room temperature to obtain the final product. For comparison, a conventional synthesis route of $NiMn_2O_4$ *via* a ball-milling method was also employed. In this method, Mn_2O_3 and $Ni(OH)_2$ were used as starting materials. Mn_2O_3 was obtained by calcining $MnCO_3$ (Kishida Chemical) at 700 °C for 12 hours. The precursors were mixed in stoichiometric ratios and calcined at several temperatures for 3 hours to synthesize $NiMn_2O_4$.

On the other hand, the conventional synthesis of P3-NiMn was carried out *via* one-step solid-state calcination for a comparison. Sodium carbonate (Nakarai Tesque), Mn_2O_3, and $Ni(OH)_2$ were used as starting materials, with Mn_2O_3 again prepared from $MnCO_3$ (Kishida Chemical) by calcination at 700 °C for 12 hours. The mixture was prepared in stoichiometric proportions, calcined at 625 °C for 15 hours, and then quenched to room temperature. Details of the synthetic procedure are summarized schematically in Fig. S1 (SI).

2.2 Material characteristics

Powder X-ray diffraction (XRD) and *ex situ* XRD measurements of electrodes were conducted using a Rigaku SmartLab X-ray diffraction system with a Bragg–Brentano optical system. A Cu tube (Cu Kα) was used as the X-ray source, with a Ni filter employed to remove the Kβ radiation. A Rigaku D/teX Ultra high-speed one-dimensional detector was used for detection. The tube current was set to 40 mA, the tube voltage to 40 kV, and the step size was 0.02°. For standard measurements, the scan speed was set to 5° per minute, while for samples requiring Rietveld analysis, the scan speed was reduced to 0.2° per minute. For *ex situ* XRD measurements, after reaching the target potential and maintaining it for 24 hours, the coin cell was disassembled under an Ar atmosphere in a glove box to extract the electrode. The electrode was cleaned with diethyl carbonate (DEC) and then dried in a glove box under an Ar atmosphere before being used as the measurement sample. For *ex situ* XRD measurements, an Al sample holder was used, with a step size of 0.02° and a scan speed of 2° per minute. For powder and electrode samples that are highly sensitive to atmospheric exposure, X-ray diffraction measurements were performed by sealing the sample plate, which held the sample, in an airtight sample holder under an Ar atmosphere inside the glove box.

Synchrotron XRD (SXRD) measurements were conducted using the BL02B2 beamline at SPring-8. For the SXRD sample preparation, a few milligrams of powder were encapsulated in a Hilgenberg φ0.03 mm Lindemann glass capillary. The

This journal is © The Royal Society of Chemistry 2026

J. Mater. Chem. A, 2026, **14**, 5626–5638 | **5627**

opening of the capillary was then sealed with Busbond. To completely prevent atmospheric exposure, after sealing, the capillary was taken out of the glove box, and the part of the capillary about 4 cm from the tip was heated and burned off before performing the measurement. Structural parameters were refined by the Rietveld method with the program RIETAN-FP and schematic illustrations of the crystal structures of the sample were drawn using the program VESTA.

Scanning electron microscopy (SEM) images were obtained using a JEOL JMC-6000 microscope, and energy dispersive X-ray spectroscopy (EDS) was conducted using a JEOL JED-2300 series. The imaging was performed with an acceleration voltage of 15 kV. The observations were carried out on powder samples, which were mounted directly onto carbon tape. Cross-sectional SEM images were observed on samples that were pre-milled using a Cross-Section Polisher (CP, JEOL IB-19530CP). The acceleration voltage during milling was set to 4.5 kV. SEM observations were conducted using a JEOL JSM-IT800SHL, and the acceleration voltage was typically set to 1 kV.

Transmission electron microscopy (TEM)/scanning TEM (STEM) images were obtained using a JEOL JEM-ARM200F (HR) microscope based on sectional annular dark field (ADF), part of the NIMS Battery Research Platform, with an acceleration voltage of 200 kV. The observations were carried out on electrode samples that were processed to a thickness of approximately 100 nm using a Hitachi High-Technologies SMF2000 focused ion beam (FIB)-SEM system. EDS and electron energy-loss spectroscopy (EELS) measurements were also conducted using the same system at 200 kV. The energy scale of all EELS spectra was calibrated with reference to the zero-loss peak. Laser diffraction/scattering particle size distribution (PSD) measurements were performed using a Horiba Scientific Partica mini LA-350 laser diffraction/scattering particle size distribution analyzer. The dispersion medium was ion-exchanged water, with a refractive index of 1.330 for water and 1.500 for the sample. Crystal structure modeling was performed using VESTA, and Rietveld analysis of the samples measured at SPring-8 was carried out using RIETAN-FP. The wavelength of the synchrotron X-ray was calibrated using NIST SRM CeO_2 ($a = 5.41111$ [Å]), and a pseudo-Voigt function was used for the profile function. The attribution of selected area diffraction (SAED) patterns was performed using SingleCrystal.

2.3 Electrode manufacturing

The active material and acetylene black (AB) were mixed using an agate mortar and pestle at a weight ratio of 80 : 10 (wt%). The resulting powder mixture was then dispersed in an N-methyl-pyrrolidone (NMP, Kanto Chemical Co., Ltd) solution in which polyvinylidene fluoride (PVdF) had been previously dissolved. The amount of PVdF was set to be equal in weight to that of AB (*i.e.*, 10 wt% relative to the active material). The slurry was further dispersed and kneaded using an ointment container containing six agate beads (φ 2 mm), followed by processing with a planetary centrifugal mixer (ARE-310, THINKY). The prepared slurry was cast onto an aluminum foil current collector using a doctor blade, and dried under reduced

pressure at 100 °C. After drying, the electrode film was punched into disk shapes with diameters of either 10 mm or 15 mm and used for electrochemical testing. The punched electrodes were sandwiched between two pieces of titanium (Ti) foil and subjected to hydraulic pressing at 1 ton for 2.5 minutes before measurement. The electrode exhibited an active material loading of $\sim$1.3 mg cm^{-2}.

2.4 Electrochemical tests

Constant current charge–discharge tests were performed on P3-NiMns synthesized by two different methods. The conditions used for these tests were as follows: the coin cells used were R2032-type. The counter electrode was sodium metal, and the electrolyte consisted of 1 mol dm^{-3} NaPF$_6$ in propylene carbonate (PC) with 2 vol% fluoroethylene carbonate (FEC). The current density was set to C/10, where 1C is equivalent to 260 mA h g^{-1}, and the voltage range was between 1.5 V and 4.5 V (*vs.* Na). The tests were performed at room temperature (25 °C), and glass separators were used in the coin cells. A rest time of 5 minutes was implemented between charge and discharge cycles. For rate tests, the charging process was fixed at C/10 (1C = 260 mA g^{-1}), and the discharge process was evaluated by gradually increasing the current density from C/10 to C/5, 1C, 2C, and 4C every 5 cycles.

For *operando* XRD measurements, a cell from EC Frontier equipped with a Be window was used. By irradiating X-rays into the cell through the Be window located at the top of the cell, it is possible to observe the crystallographic changes in the cathode active material during the sodium de-insertion and insertion process. The assembly of the cell was performed entirely within a glove box. No reference electrode was used in this study. The *operando* XRD measurements were conducted using a Rigaku MultiFlex equipped with a high-speed 1D semiconductor detector (D/teX Ultra) and measured with a Bragg–Brentano optical system. A Cu X-ray tube (Cu Kα) was used as the X-ray source, and a Ni filter was employed to remove the Kβ radiation. The tube voltage was set to 40 kV, and the tube current was set to 30 mA. The step width was set to 0.02° and the scan speed was set to 3° per minute as a standard. A three-electrode cell from EC Frontier, also equipped with a Be window, was used for the charge–discharge measurements.
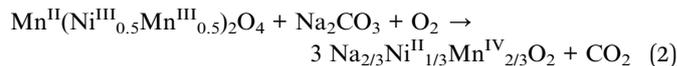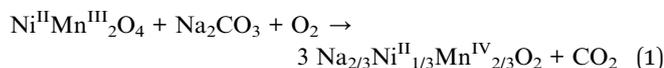
3 Results and discussion

Optimization and development of synthesis processes have been actively pursued to tune the physicochemical properties and electrochemical performance of electrode materials. For example, since our group first reported P2-Na$_{2/3}$[Fe$_{1/2}$Mn$_{1/2}$]O$_2$ synthesized *via* a solid-state reaction as a new positive electrode material for NIBs in 2012,[26] Li *et al.* developed a novel low-temperature eutectic synthesis route to enhance Na-ion diffusivity and reaction kinetics, along with improving homogeneity, crystallinity, and purity.[27] Additionally, Manthiram *et al.* demonstrated a two-step molten salt synthesis using sodium chloride and metal oxides to obtain layered O3-type Na(Ni$_{0.3}$Fe$_{0.4}$Mn$_{0.3}$)O$_2$ single crystals with significantly improved cycling

5628 | *J. Mater. Chem. A*, 2026, **14**, 5626–5638

This journal is © The Royal Society of Chemistry 2026

stability and air resistance.[28] This method involved the formation of micron-sized truncated octahedral single crystals of a mixed-phase spinel/rock-salt intermediate, which served as an effective precursor for the subsequent formation of the material with large primary particles and extended cycle life. On the other hand, Bianchini *et al.* demonstrated, through real-time measurements, that the layered $LiCoO_2$ oxide was formed by passing through several spinel phases from β-$Co(OH)_2$ and spinel-type Co_3O_4 precursors.[29] This study suggested the possibility of using spinel structures as precursors for synthesizing layered oxide phases. From this perspective, this study developed a novel synthetic approach employing spinel-type highly crystalline $NiMn_2O_4$ as a key starting precursor, which then undergoes a solid-state reaction with a sodium source at a lower temperature of 625 °C to yield the desired P3-NiMn. Further details of the synthesis process are described in the Experimental section and in the SI (Fig. S1).

3.1 Designing an optimal spinel-type $NiMn_2O_4$ precursor

Fig. 1a illustrates the expected formation pathways of P3-NiMn, synthesized from spinel (or inverse spinel) $NiMn_2O_4$. The reaction pathways are presumed to proceed as follows:

$$Ni^{II}Mn^{III}_2O_4 + Na_2CO_3 + O_2 \rightarrow$$
$$3\ Na_{2/3}Ni^{II}_{1/3}Mn^{IV}_{2/3}O_2 + CO_2 \quad (1)$$

$$Mn^{II}(Ni^{III}_{0.5}Mn^{III}_{0.5})_2O_4 + Na_2CO_3 + O_2 \rightarrow$$
$$3\ Na_{2/3}Ni^{II}_{1/3}Mn^{IV}_{2/3}O_2 + CO_2 \quad (2)$$

This indicates that 1 mol of $NiMn_2O_4$ requires 2 mol of Na^+ and 1 mol of O_2 along with 1 electron oxidation to fully convert into the layered oxide phase. To obtain the advanced P3-type NiMn which overcomes the aforementioned inherent limitations, such as low crystallinity, as the final target material, we first aimed to design the optimal spinel-type $NiMn_2O_4$ precursor using both conventional ball-milling (BM) and spray-drying (SD) methods with varying calcination temperatures. Fig. 1b shows the XRD patterns of the synthesized spinel-type $NiMn_2O_4$ materials. Here, the samples are denoted as (BM or SD)-x, where x indicates the calcination temperature in degrees Celsius. For the samples prepared *via* the SD method, XRD patterns up to SD-1200, as well as that of BM-1000, could be indexed to a cubic spinel structure with the $Fd\bar{3}m$ space group, confirming the successful formation of spinel-type oxides. However, in SD-1300 and BM-1100, additional peaks corresponding to NiO were observed, indicating that single-phase spinel $NiMn_2O_4$ was not achieved in these samples. Notably, the spinel phase was preserved at higher temperatures in the SD method compared to the BM method. This is likely due to the superior homogeneity of the precursor mixtures prepared by spray drying.[30,31] In the BM method, precursors are mechanically mixed as solid powders, leading to less uniformity and more defects, which
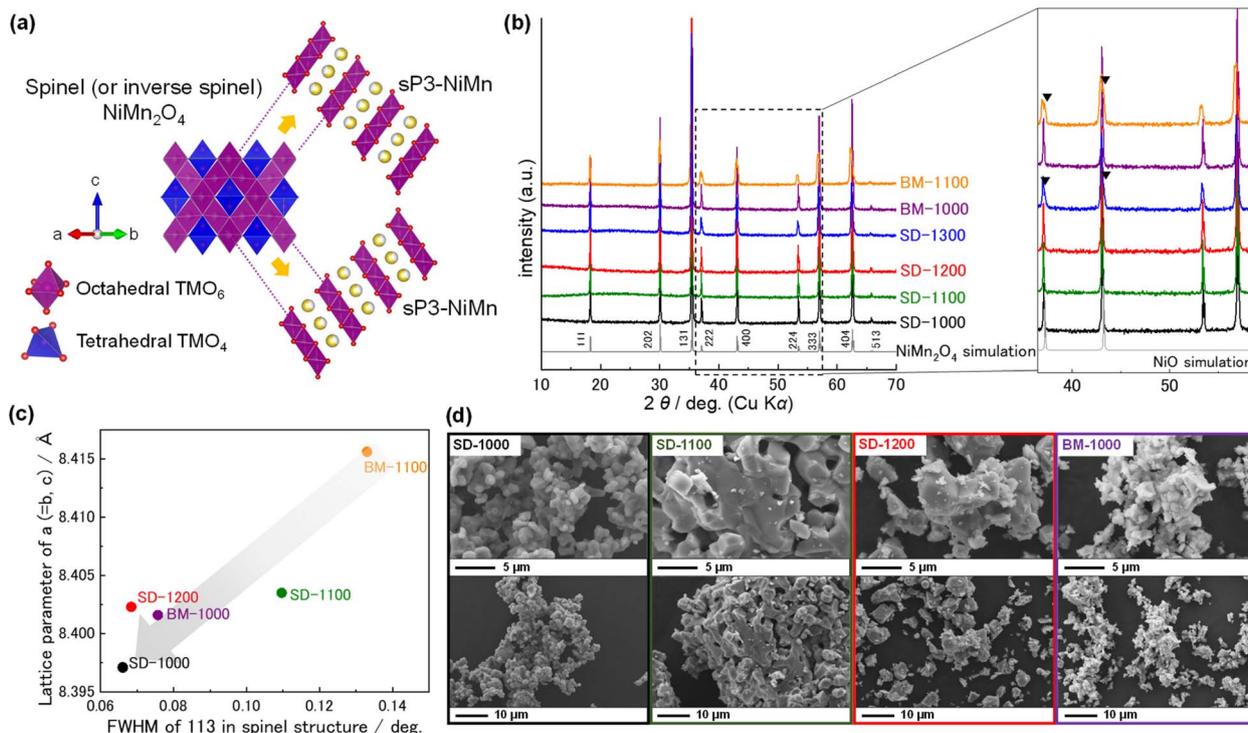

Fig. 1 Structural/morphological characteristics of spinel-type $NiMn_2O_4$. (a) Schematic illustration of the phase transition process from spinel $NiMn_2O_4$ to P3-NiMn. (b) XRD patterns of spinel $NiMn_2O_4$ powders synthesized *via* spray-drying and ball-milling methods at various calcination temperatures. (c) Plots of the FWHM of the 113 XRD peak *versus* the lattice parameter for the single-phase samples, estimated from (b). (d) SEM images of synthesized spinel-type $NiMn_2O_4$ powders.

This journal is © The Royal Society of Chemistry 2026

J. Mater. Chem. A, 2026, **14**, 5626–5638 | **5629**

can inhibit high-quality crystal formation. In contrast, the solution-based SD method involves atomizing a precursor solution into fine droplets followed by rapid drying, resulting in powders with significantly enhanced compositional homogeneity. This improved uniformity can contribute to the formation and retention of a single-phase spinel structure at elevated temperatures in SD-derived samples, in contrast to the BM-derived counterparts.

Fig. 1c presents a plot of the full width at half maximum (FWHM) of the 113 XRD peak (*x*-axis) *versus* the lattice parameter (*y*-axis) for the single-phase samples, based on Fig. 1b and Table S1, providing a clear comparison of crystallinity and structural characteristics. Among the samples, SD-1000 exhibited the narrowest FWHM of the 113 peak, indicating the highest crystallinity, which is expected to contribute to the formation of a highly crystalline final P3-NiMn phase. In contrast, the samples calcined at excessively high temperatures (*e.g.*, SD-1200 and SD-1300) exhibited reduced crystallinity, which is likely attributed to partial decomposition of the spinel phase, cation disordering, and microstructural instability induced by thermal stress and sintering.[32,33] In addition, the corresponding *a*-axis lattice parameter in SD-1000 was the smallest, approximately 8.397 Å, which is consistent with previously reported values.[34,35] A reduced lattice parameter in the spinel precursor implies a denser cationic framework, which may promote the formation of a more ordered layered structure during the phase transformation to the P3-type structure. Furthermore, the SEM images of the single-phase samples are shown in Fig. 1d. The SD-1000 sample exhibited uniformly distributed primary particles with an average size of approximately 2 μm. In contrast, SD-1100 and SD-1200 showed aggregates formed by the fusion of larger sized particles with decreased uniformity, which may be due to incomplete crystal growth, consistent with their broader FWHM (Fig. 1c). BM-1000, on the other hand, exhibited smaller and less uniform particles compared to the SD-derived samples. The crystallite size, estimated using Scherrer's equation based on the 311 diffraction peak, was 122 nm for SD-1000, larger than the 113 nm for BM-1000. This difference is also attributed to the enhanced homogeneity of the precursor materials in the SD method. Consequently, based on the comprehensive results including phase purity, crystallinity, particle morphology, and crystallite size, SD-1000 could be considered the most promising precursor for the synthesis of the targeted P3-type NiMn materials with enhanced crystallinity and uniformity.

3.2 Structural/morphological characteristics of spinel-driven P3-NiMn

A synchrotron XRD pattern with Rietveld analysis of spinel-type $NiMn_2O_4$ powder (SD-1000) used as a precursor is shown in Fig. 2a, indicating that the crystal structure of SD-1000 corresponds to an inverse spinel configuration. The details for the Rietveld refinement results are exhibited in Table S2. The single-phase spinel structure identified in the conventional XRD pattern (Fig. 1b) was consistently confirmed by synchrotron XRD, further validating the phase purity and crystallographic assignment.[30,31] Next, synchrotron XRD patterns are

shown in Fig. 2b for both the two-step spinel-derived P3-NiMn using SD-1000 and a one-step conventional P3-NiMn (hereafter referred to as "sP3-NiMn" and "cP3-NiMn", respectively) with their Rietveld refinement results (Fig. S2, S3 and Tables S3, S4). For both samples, the main diffraction peaks were indexed to a rhombohedral structure with space group $R3m$, confirming that both samples exhibit a P3-type layered structure. Additionally, the refined lattice parameters were consistent with previous reports, indicating successful synthesis of P3-type materials comparable to those previously reported.[17] Notably, the inset of Fig. 2b shows the normalized 003 reflection peak, which exhibited a narrower FWHM for the 003 peak in sP3-NiMn than in cP3-NiMn, corresponding to crystallite sizes of 43.5 nm and 32.1 nm, respectively. As a result, the above findings indicate that sP3-NiMn can be successfully derived from inverse spinel $NiMn_2O_4$ through the process described in eqn (2), exhibiting high crystallinity and a large crystallite size.

During the phase transformation of the spinel-type oxide to the layered structure, lattice distortion and intra-particle cracking can occur, potentially leading to reduced crystallinity. However, XRD results demonstrated that employing a highly crystalline spinel-type oxide as a precursor enabled the successful synthesis of a P3-type layered oxide with high crystallinity and large crystalline size, especially towards *c*-axis ordering. Regarding the lattice parameters, the *a*-axis length of sP3-NiMn was slightly larger than that of cP3-NiMn, while its *c*-axis length was shorter, which is likely attributed to the formation of NiO. As shown in the XRD pattern of sP3-NiMn, in contrast to cP3-NiMn, an additional diffraction peak was observed near 13.5°, identified as a minor NiO phase. According to the refinement results (Fig. S3 and Table S4), the weight ratio of the P3-type oxide to NiO in sP3-NiMn was found to be 97 : 3. This NiO phase is presumed to originate from the decomposition of the spinel precursor during synthesis, despite the use of a single-phase spinel $NiMn_2O_4$ precursor, and its influence on the structural and electrochemical properties of P3-NiMn will be discussed in more detail later.

As shown in the SEM images in Fig. 2b, sP3-NiMn exhibits well-formed primary particles with larger size, approximately 2 μm in diameter, which is identical to that of the $NiMn_2O_4$ (SD-1000) precursor (Fig. 1d). In contrast, the cP3-NiMn sample consisted of aggregates of smaller primary particles with sizes in the range of 200–400 nm, which is consistent with the particle-size distribution results (Fig. S4). These results suggest that using a spinel-type oxide as the precursor leads to an increase in the final particle size of the resulting P3-NiMn. Furthermore, Fig. 2c presents cross-sectional ADF-STEM and EDS mapping images of P3-NiMns for the Ni K-edge. The corresponding EELS spectra for the Ni L-, Mn L-, and O K-edges are shown in Fig. 2d. Additional elemental analyses, including EDS spectra, are provided in Fig. S5 and S6, while the SAED patterns corresponding to the STEM images are shown in Fig. S7. As mentioned earlier, the differences in particle sizes between cP3-NiMn and sP3-NiMn could also have been observed in STEM images (Fig. 2c). Additionally, the particles exhibited internal voids approximately 200 nm in diameter in cP3-NiMn, which differ from those in sP3-NiMn. Notably, bright regions within
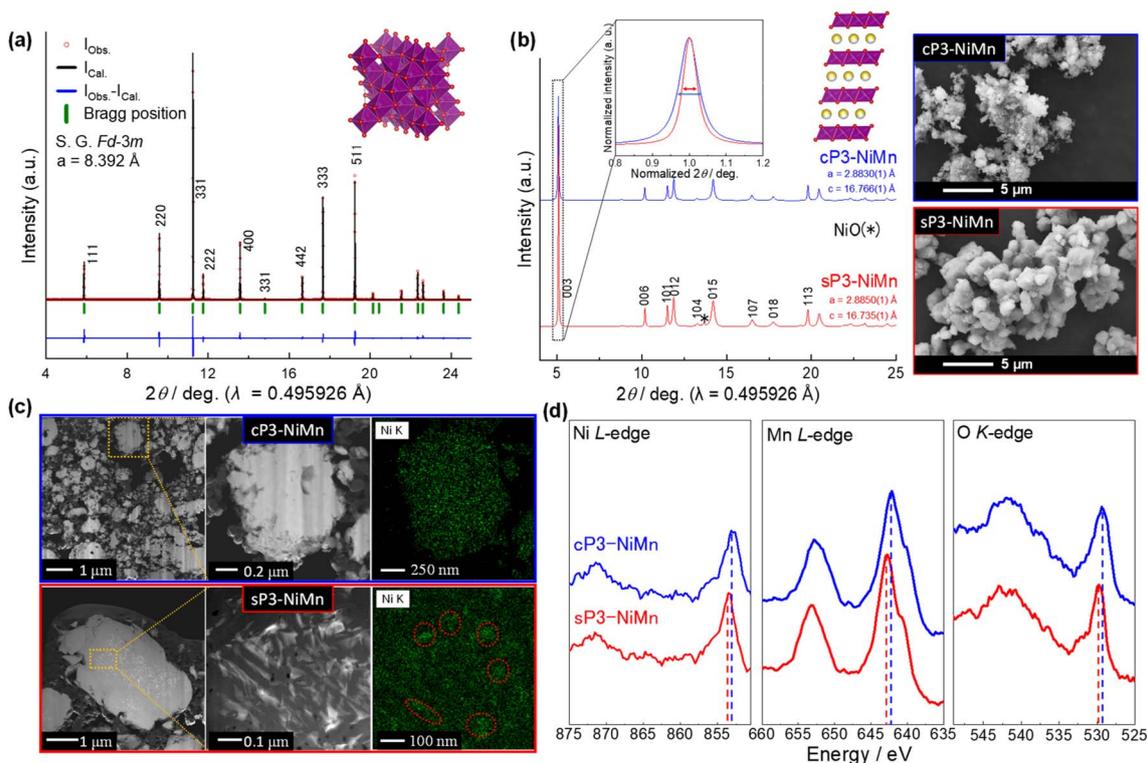
5630 | *J. Mater. Chem. A*, 2026, **14**, 5626–5638

This journal is © The Royal Society of Chemistry 2026

Fig. 2 Structural/morphological characteristics. (a) Rietveld refinement results on a synchrotron XRD pattern of spinel–type $NiMn_2O_4$ powder (SD-1000). (b) Synchrotron XRD patterns and SEM images of cP3-NiMn and sP3-NiMn powders. (c) ADF-STEM and EDS mapping images of the Ni K edge of cP3-NiMn and sP3-NiMn powders. (d) EELS spectra of Ni L-, Mn L-, and O K-edges of cP3-NiMn and sP3-NiMn powders within the bulk region.

the bulk particles of sP3-NiMn were observed in the STEM image (Fig. 2c), where EDS mapping revealed significant Ni enrichment (highlighted by circles), while the cP3-NiMn sample exhibited a uniform elemental distribution of O, Na, Mn, and Ni across the particles (Fig. S5). Moreover, EDS spectra from normal (non-bright) regions showed stronger Mn signals than Ni, consistent with the intended composition, while the spectra from the bright regions revealed higher Ni counts than Mn (Fig. S6), indicating a clear deviation from the target stoichiometry. These Ni-rich regions are associated with the NiO phase identified in the XRD pattern (Fig. 2b).

According to previous EELS studies, the position of the Ni L_3 absorption edge varies depending on the oxidation state of Ni: for NiO (Ni^{2+}), and the peak appears at 854 eV; for $LiNiO_2$ (Ni^{3+}) and NiO_2 (Ni^{4+}), the peaks are observed at 855 eV and 857 eV, respectively.[36–38] In the present study, the cP3-NiMn sample showed a Ni L_3-edge peak at around 854 eV, consistent with Ni^{2+} (Fig. 2d). In contrast, the sP3-NiMn sample exhibited a slight shift of the Ni L_3 peak toward higher energy, along with similar shifts observed for the Mn and O edges. As confirmed by XRD and Rietveld refinement, the weight ratio of the P3-type oxide to NiO in sP3-NiMn was determined to be 97 : 3 (m m^{-1}), corresponding to an approximate molar ratio of 96 : 4 (mol mol^{-1}). Based on this result, the composition of sP3-NiMn can be estimated as $Na_{0.70}[Ni_{0.30}Mn_{0.70}]O_2$, which is slightly off-stoichiometry of Ni and slightly Mn and Na-rich compared

with $Na_{0.667}[Ni_{0.333}Mn_{0.667}]O_2$. In this composition, the average oxidation state of Mn should decrease from +4.00 to approximately +3.86, indicating the presence of a small fraction of Mn^{3+}, resulting in the formation of P3-type $Na_{0.70}[Ni^{II}_{0.30}Mn^{IV}_{0.60}Mn^{III}_{0.10}]O_2$ containing 3 wt% NiO. It is thus probable that the observed high-energy shift of the EELS spectrum of the Mn L-edge is attributed to local Jahn–Teller distortions induced by Mn^{3+} ions. As is generally known, the energy shift in the EELS spectrum is primarily governed by changes in the electronic structure. However, such shifts can be correlated with variations in TM–O bond lengths, as these structural changes influence the local electronic environment. In this context, the shift observed in the Mn L-edge spectrum can reflect the elongation or compression of Mn–O bonds due to local Jahn–Teller distortions. Consequently, the presence of Mn^{3+} ions can alter the local symmetry and electronic structure of the MnO_6 octahedra, leading to a modification in the energy distribution of unoccupied Mn 3d orbitals and a consequent shift of the Mn L-edge.[39,40] A similar effect may also influence the Ni-L and O-K edges due to modified hybridization and local electronic redistribution.

3.3 Electrochemical performances

Fig. 3 shows the electrochemical performance of cP3-NiMn and sP3-NiMn in Na//P3-NiMn half-cells. In the voltage range of 1.5–4.0 V shown in Fig. 3a–c, while both cP3-NiMn and sP3-NiMn
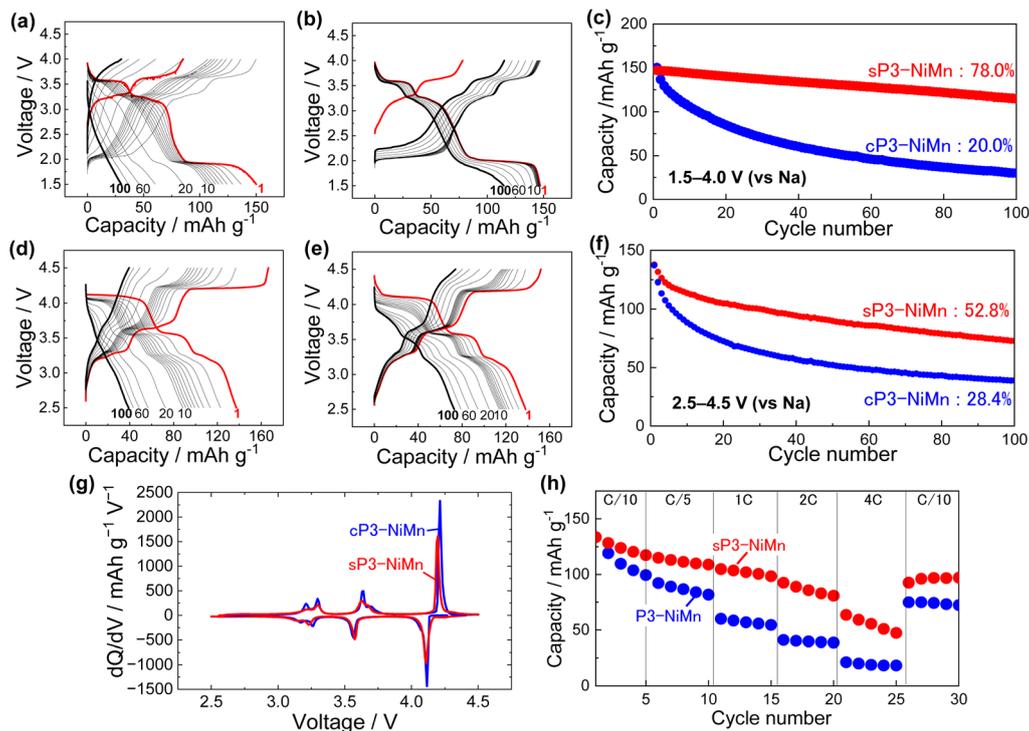
Fig. 3 Electrochemical performances. (a)–(f) Cycle performance of cP3-NiMn and sP3-NiMn electrodes in 1 mol dm^{-3} NaPF$_6$/PC with 2 vol% FEC at C/10 (1C = 260 mA g^{-1}) within voltage ranges of (a)–(c) 1.5–4.0 V (*vs.* Na) and (d)–(f) 2.5–4.5 V (*vs.* Na). (g) Differential capacity (dQ/dV) plots of cP3-NiMn and sP3-NiMn electrodes during the first cycle within the voltage range of 2.5–4.5 V (*vs.* Na). (h) Rate capability of cP3-NiMn and sP3-NiMn in 1 mol dm^{-3} NaPF$_6$/PC with 2 vol% FEC in the voltage range of 2.5–4.5 V (*vs.* Na), measured at various C-rates (1C = 260 mA g^{-1}).

exhibited similar voltage profiles and capacities during the initial cycles, a significant performance difference was observed after 100 cycles with sP3-NiMn retaining a much higher capacity. Similar trends were found when the voltage range was changed to 2.5–4.5 V (Fig. 2d–f) as well as in the narrow range of 2.5–4.1 V (Fig. S8). These results indicate that employing spinel-type NiMn$_2$O$_4$ as a precursor significantly improves the cycling performance of P3-NiMn by altering its physicochemical properties, as demonstrated above.

On the other hand, the slight off-stoichiometry of sP3-NiMn can influence the charge–discharge behavior. The reduction in initial capacity observed for sP3-NiMn is most likely associated with the presence of electrochemically inactive NiO. Indeed, sP3-NiMn delivered an initial charge capacity of ~152 mA h g^{-1} within 2.5–4.5 V (Fig. 2e), which is in close agreement with the theoretical value (~154 mA h g^{-1}) predicted from Ni redox in Na$_{0.70}$[Ni$_{0.30}$Mn$_{0.70}$]O$_2$. Moreover, the reduced initial discharge capacity within 1.5–4.0 V (Fig. 2e), where the Mn$^{4+/3+}$ redox couple is active, can also be attributed to the decreased fraction of Mn^{4+} in sP3-NiMn. This overall consistency further supports our interpretation of the off-stoichiometry estimated by Rietveld refinement.

Although sP3-NiMn exhibited more stable cycling in the 1.5–4.1 V (*vs.* Na) range as shown above, the 2.5–4.5 V (*vs.* Na) range can be considered more proper for practical high-energy density NIB applications.[41,42] Therefore, the following sections will focus primarily on the electrochemical results obtained within

the voltage range. Fig. 3g presents differential capacity (dQ/dV) plots of cP3-NiMn and sP3-NiMn electrodes. In these profiles, sharp redox peaks were observed for stoichiometric cP3-NiMn, corresponding to its phase transition. Notably, although the voltage regions and overall peak behaviors of cP3-NiMn and sP3-NiMn remained nearly identical, which is likely because fundamental structural features, such as the presence of the superlattice, are only minimally affected by such minor compositional deviations with slight Mn-rich stoichiometry,[43,44] the redox peaks for sP3-NiMn appeared broader. This broadening is presumably due to the suppression of rapid phase transition processes, as well as local structural heterogeneity induced by compositional deviations in sP3-NiMn, which results in a distribution of redox potentials. These aspects will be further discussed in the *operando* XRD results presented in the next section.

On the other hand, as shown in Fig. S9, no significant effect was observed for "P2"-NiMn, even though the same spinel-type NiMn$_2$O$_4$ precursor and synthesis process were applied except for the final calcination temperature (900 °C) required to form the P2 structure. This is likely because the higher calcination temperature itself contributes to the high crystallinity of the P2-type materials, regardless of whether the spinel-type NiMn$_2$O$_4$ precursor is used. Consequently, this novel synthesis method is not suitable for P2-NiMn, but rather effective specifically for P3-NiMn materials. We believe that not only the low temperature process but also the similar oxide anion packing of the P3/O3-

5632 | *J. Mater. Chem. A*, 2026, **14**, 5626–5638

This journal is © The Royal Society of Chemistry 2026

type structure to that of spinel phase play a key role in enhancing P3-type electrode behavior. Furthermore, Fig. 3h and S10 show rate capability results for both cP3-NiMn and sP3-NiMn within the 2.5–4.5 V range. sP3-NiMn consistently delivered higher capacity than cP3-NiMn across all rates. Based on these comparisons, the sP3-NiMn developed in this study exhibits significantly enhanced electrochemical performance, including superior cycling stability and rate capability, which could be closely associated with its unique physicochemical features. The details will be further elucidated through the mechanistic analysis presented below.

3.4 Mechanism of performance improvement

As discussed above, differences between cP3-NiMn and sP3-NiMn were observed in terms of cycling performance, rate capability, as well as structural, compositional and morphological features. To investigate the mechanisms underlying the enhanced electrochemical performance, *operando* XRD measurements were first conducted during the initial cycle. Fig. 4 presents the *operando* XRD patterns of cP3-NiMn (Fig. 4a) and sP3-NiMn (Fig. 4b), along with their corresponding charge–discharge curves. As shown in Fig. 4a, cP3-NiMn undergoes a clear phase transition sequence of P3 → P3 + O1 → O3 + P3 → O3 during charging, which reverses during discharge. In contrast, in sP3-NiMn, the O3 phase appeared only slightly near the very end of the charging processes (a magnified view of

Fig. 4b is provided in Fig. S11), indicating that the phase transition to O3 was largely suppressed. Additionally, the phase transition of sP3-NiMn appears to be somewhat smoother, whereas cP3-NiMn exhibits an abrupt and instantaneous phase transition. This likely results from the physicochemical differences of sP3-NiMn and cP3-NiMn. As demonstrated by the XRD results (Fig. S3), the sP3-NiMn phase is of non-stoichiometric composition with 3 wt% NiO despite phase-pure stoichiometric cP3-NiMn, so that sP3-NiMn exhibited a slight contraction along the *c*-axis and an expansion along the *a*-axis, suggesting a reduction in interlayer O⋯O repulsion along the *c*-axis between TMO$_2$ slabs. These structural characteristics affect phase transitions and, in turn, play a definitive role in enhancing the cycling stability of the material, as a severe phase transition as well as lattice volume change is one of the primary causes of capacity degradation in electrode materials.

Next, the crystal structures of both samples after 100 cycles within the 2.5–4.5 V range were investigated by XRD measurements (Fig. 5a). sP3-NiMn retained sharp and well-defined diffraction peaks after 100 cycles, indicating that the P3-type structure was largely preserved. In contrast, cP3-NiMn exhibited a reversal in the intensity ratio between the 101_{P3} and 012_{P3} peaks, suggesting that the layered structure had been disrupted. These trends were also supported by the apparent crystallite sizes calculated from the 003 reflections before and after 100 cycles (Fig. 5b), which show that the crystallite size of sP3-NiMn
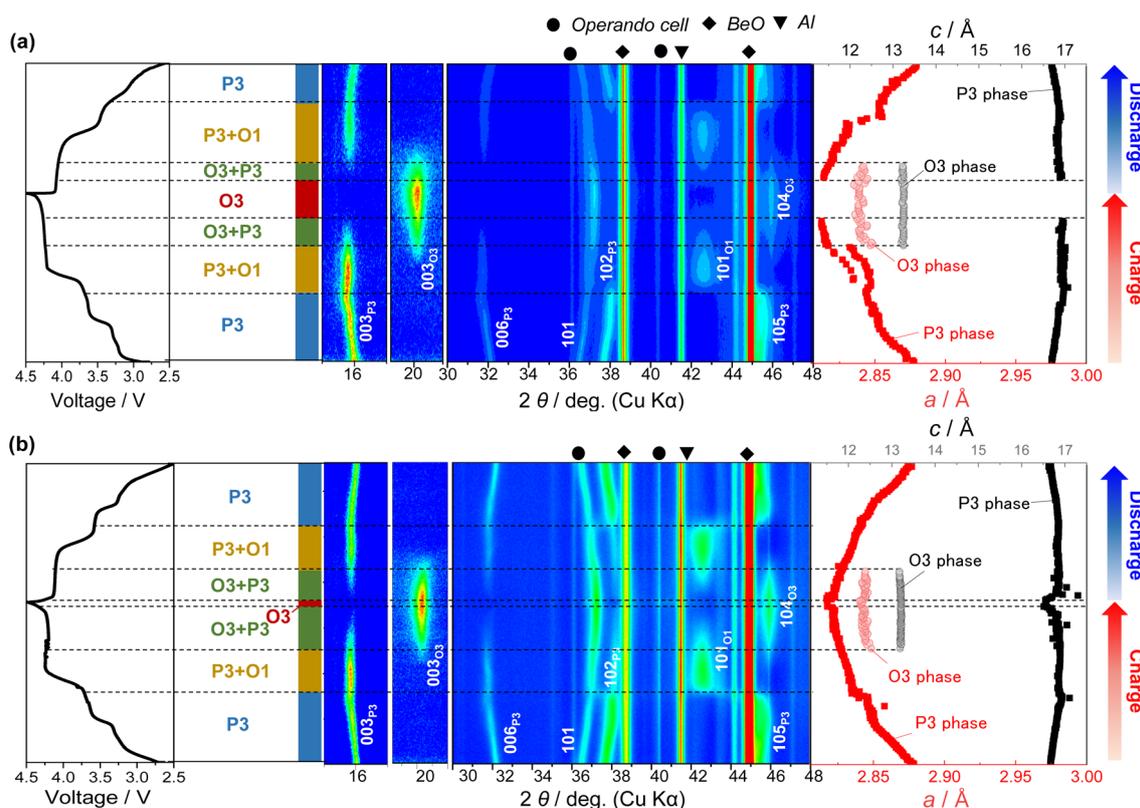

Fig. 4 *Operando* structural observations during the initial cycle. *Operando* XRD patterns, corresponding charge/discharge curves, and lattice parameter evolution of (a) cP3-NiMn and (b) sP3-NiMn electrodes tested in 1 mol dm^{-3} NaPF$_6$/PC with 2 vol% FEC in the voltage range of 2.5–4.5 V (*vs.* Na) during the initial cycle.

This journal is © The Royal Society of Chemistry 2026

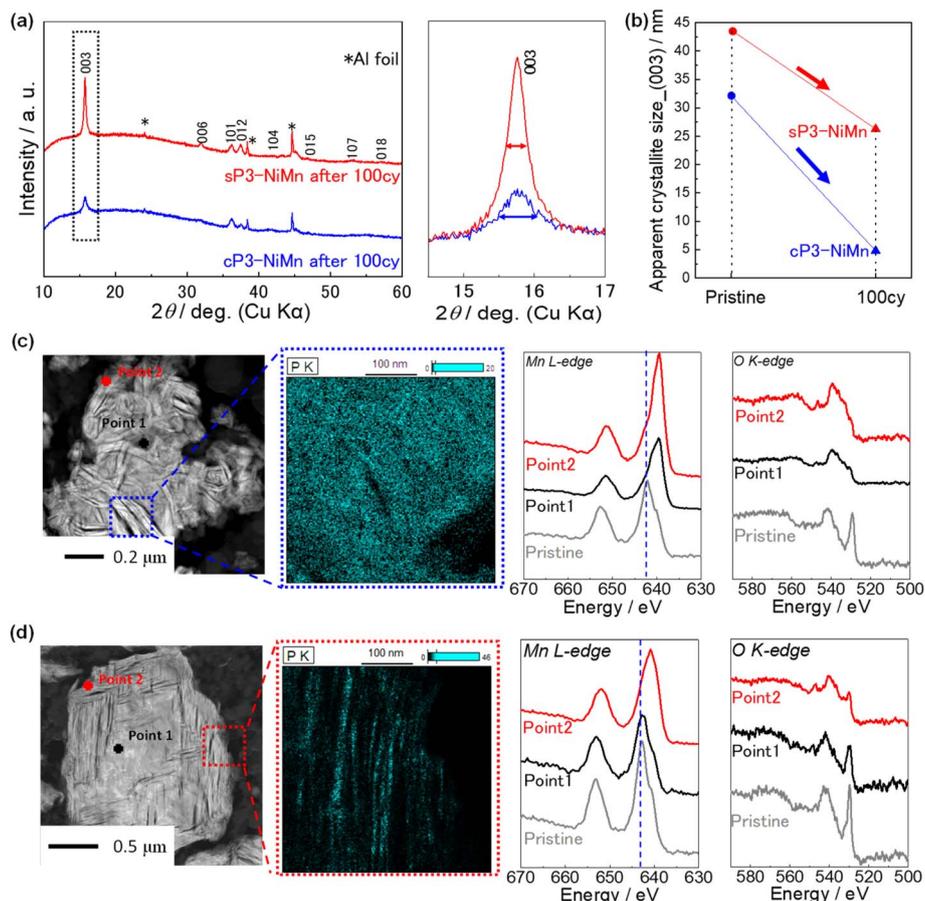*J. Mater. Chem. A*, 2026, **14**, 5626–5638 | **5633**

Fig. 5 Post-cycling structural characterization. (a) XRD patterns of cP3-NiMn and sP3-NiMn electrodes after 100 cycles. (b) Comparison of apparent crystallite size changes from the pristine state to that after 100 cycles, estimated from the (003) reflections in the XRD patterns. (c) and (d) ADF-STEM images with P K-edge EDS elemental mapping and EELS spectra of the Mn L-edge and O K-edge for (c) cP3-NiMn and (d) sP3-NiMn particles after 100 cycles.

remained relatively unchanged compared to that of cP3-NiMn. It should be also noted that peak broadening is not governed solely by crystallite size. In particular, the 003_{P3} reflection exhibited more pronounced FWHM changes than other reflections, implying that microstrain broadening also contributes. This point will be discussed in detail later.

Furthermore, cross-sectional STEM analysis was also conducted to assess microstructural evolution after cycling, and the ADF-STEM images with EELS spectra are shown in Fig. 5c and d. The EDS mapping images and spectra are shown in Fig. S12–S15 and the EELS spectra of the Ni L-edge are also presented in Fig. S16. In Fig. 5c, the cP3-NiMn particle after electrochemical cycling exhibited crack formation in multiple directions, with fractures extending throughout the particle interiors. These extensive internal cracks suggest a higher degree of structural degradation caused by the lattice volume change. Additionally, based on the EELS results, the Mn L-edge shifted toward lower energy and the O K pre-edge intensity, originating from the transition between hybridized O 1s–TM 3d orbitals and the O 2p valence band states,[45,46] was also reduced after cycling in both the particle interior (point 1) and surface (point 2) in the images. Particularly, the decrease in O K pre-edge intensity is

highly related to TM migration because it disrupts the TM–O bonding network, thereby diminishing the unoccupied states associated with O 2p–TM 3d hybridization.[45,46] Moreover, its EDS mapping images in Fig. S12 showed that the phosphorus-based composition produced by electrolyte decomposition during the cycling was evenly distributed inside the cP3-NiMn particle, indicating that the electrolyte can penetrate into the particle through the formed crack. These results thus highlight that structural degradation severely compromises the electrochemical properties of cP3-NiMn, which is closely related to the severe phase transition, TM migration, the formation of particle cracks, and accelerated electrolyte decomposition across the whole particle.

On the other hand, noticeable cracks in individual particles were confirmed after 100 cycles even in sP3-NiMn. However, interestingly, these cracks were mainly formed only in the outer area of particles and appeared to propagate along a specific crystallographic direction (Fig. 5d and S17). This directional cracking behavior is likely associated with the preferred orientation of sP3-NiMn, which causes the particles to undergo anisotropic lattice expansion and contraction during Na⁺ insertion and extraction. In other words, the orientation of
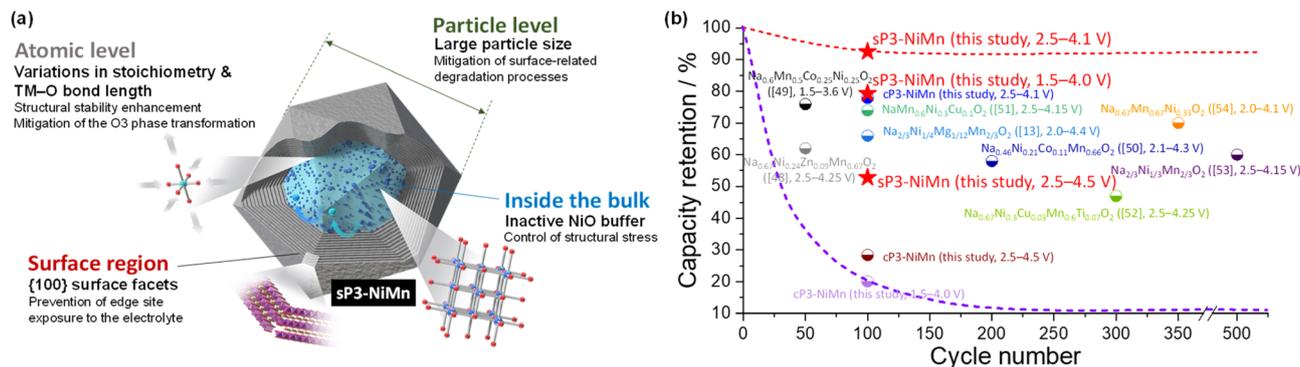
5634 | *J. Mater. Chem. A*, 2026, **14**, 5626–5638

This journal is © The Royal Society of Chemistry 2026

Fig. 6 Superiority of spinel–driven P3–NiMn. (a) Schematic illustration of the performance enhancement in sP3–NiMn. (b) Comparison of cycle performance of P3-type positive electrode materials reported in previous studies and in this work, evaluated over various voltage ranges.[13,48–54]

cracks formed at the sP3-NiMn surface indicates its assignment of {100} surface facets, since the pronounced contraction along the c-axis during the P3 → O3 transition inevitably drives crack propagation parallel to the a–b plane. In addition, we thought that redox-inactive NiO can have a positive role in maintaining the particle structure by acting as a structural buffer.[47] Additionally, the shift of the Mn L-edge peak and intensity decrease of the O K pre-edge peak in EELS spectra were observed not in point 1 (bulk) but in point 2 (surface). Notably, the O K-edge spectrum of cycled sP3-NiMn was markedly different from that of cP3-NiMn, suggesting that TM migration can be mitigated in sP3-NiMn to a noticeable extent. Furthermore, in contrast to cP3-NiMn, the phosphorus-based composition was only present at the surface, and not in the bulk (Fig. S15). As a result, these observations suggest that while sP3-NiMn maintains structural integrity and chemical uniformity over extended cycling, cP3-NiMn undergoes more extensive degradation at both the structural and compositional levels.

Taken together, the plausible effects of the designing strategy for high performance P3-NiMn on enhancing the electrochemical properties are illustrated and summarized in Fig. 6. By utilizing highly crystalline and large-sized spinel-type $NiMn_2O_4$ as a precursor, we successfully synthesized P3-type NiMn with improved crystallinity, a preferred crystallographic orientation, and enlarged particle size. During heating of a stoichiometric mixture of $NiMn_2O_4$ and Na_2CO_3, the structural transition from the spinel to the P3-layered phase occurs at 650 °C, and as a result, the octahedral arrangement of transition metals in the layered oxide is expected to inherit the framework of the spinel precursor. This inheritance likely results in a preferred orientation of the final layered phase, which can critically contribute to the improvement of rate capability by facilitating Na ion diffusion, as well as enhancing cyclability. Notably, the distinct interlayer arrangement observed in the STEM image (Fig. 5d) resulted in the formation of {100} surface facets, which are less reactive and thus suppress the exposure of edge sites to the electrolyte. This surface configuration, together with the larger particle size, contributed to mitigating surface-related degradation processes such as electrolyte decomposition and Mn dissolution. Moreover, this structural arrangement

is expected to effectively suppress crack formation induced by volume changes during cycling. Structural analysis also revealed the presence of NiO within the bulk of the particles, likely originating from Ni migration with slow kinetics from tetrahedral to octahedral sites during the phase transition. Impure NiO does not participate in redox reactions, instead acting as a buffer against structural stress from repeated volume changes. Additionally, the formation of NiO induced subtle compositional changes, leading to variations in the lattice parameters and, consequently, modifying the stoichiometry of the P3-NiMn phase. These changes can contribute to suppressing phase transitions during the charge/discharge process, as well as mitigating TM migration, significantly improving the cycle stability. Consequently, the rational design of the synthesis method can enhance the electrochemical performances of P3-type cathodes, without any additional optimization such as heteroatom doping or surface modification. Notably, as shown in Fig. 6b, the sP3-NiMn sample demonstrates superior cycling performance compared to previously reported P3-type layered oxide positive electrode materials for NIBs.[13,48–54] These results highlight the potential applicability of this material and its synthesis method for practical implementation.

4 Conclusions

This study successfully synthesized a high-performance P3-type NiMn material by utilizing an optimally designed spinel-type $NiMn_2O_4$ precursor. The resulting spinel-derived P3-NiMn exhibited unique electrode behavior differing from those of conventional P3-NiMn, including high crystallinity, a unique c-axis ordering, large particle size, the formation of NiO buffer and a basal-plane-based surface layer, and unintended compositional shift. These features significantly contributed to the improved electrochemical performance of the P3-type material, but were not applicable for the P2-type material. In particular, its cycling stability was exceptional even without any modifications, surpassing that of most previously reported P3-type materials, which is attributed to the suppression of phase transition processes, side reactions at the surface, and crack formation within the particles during electrochemical

This journal is © The Royal Society of Chemistry 2026

J. Mater. Chem. A, 2026, **14**, 5626–5638 | **5635**

cycling. Overall, these results demonstrate that our newly developed synthesis strategy enables the fabrication of high-performance P3-type materials, thereby enhancing their potential for practical application in NIBs. As future work, we plan to extend this spinel precursor-based synthesis strategy to other layered oxide positive electrode materials for NIBs, aiming to develop a broader range of high-performance P3-type compounds.

Conflicts of interest

The authors declare that they have no known competing financial interests or personal relationships that could have appeared to influence the work reported in this paper.

Data availability

The data that support the findings of this study are available from the corresponding authors upon reasonable request. Supplementary information (SI) is available. See DOI: https://doi.org/10.1039/d5ta07169k.

Acknowledgements

References

1 N. Yabuuchi, K. Kubota, M. Dahbi and S. Komaba, Research Development on Sodium-Ion Batteries, *Chem. Rev.*, 2014, **114**, 11636.

2 S. Komaba, W. Murata, T. Ishikawa, N. Yabuuchi, T. Ozeki, T. Nakayama, A. Ogata, K. Gotoh and K. Fujiwara, Electrochemical Na Insertion and Solid Electrolyte Interphase for Hard-Carbon Electrodes and Application to Na-Ion Batteries, *Adv. Funct. Mater.*, 2011, **21**, 3859.

3 M. H. Han, E. Gonzalo, G. Singh and T. Rojo, A Comprehensive Review of Sodium Layered Oxides: Powerful Cathodes for Na-Ion Batteries, *Energy Environ. Sci.*, 2015, **8**, 81.

4 J. Y. Hwang, S. T. Myung and Y. K. Sun, Sodium-ion Batteries: Present and Future, *Chem. Soc. Rev.*, 2017, **46**, 3529.

5 V. R. R. Boddu, D. Puthusseri, P. M. Shirage, P. Mathur and V. G. Pol, Layered Na$_x$CoO$_2$-based Cathodes for Advanced Na-Ion Batteries: Review on Challenges and Advancements, *Ionics*, 2021, **27**, 4549.

6 S. W. Kim, D. H. Seo, X. Ma, G. Ceder and K. Kang, Electrode Materials for Rechargeable Sodium-Ion Batteries: Potential Alternatives to Current Lithium-ion Batteries, *Adv. Energy Mater.*, 2012, **2**, 710.

7 C. Delmas, Sodium and Sodium-Ion Batteries: 50 Years of Research, *Adv. Energy Mater.*, 2018, **8**, 1703137.

8 C. Delmas, C. Fouassier and P. Hagenmuller, Structural Classification and Properties of the Layered Oxides, *Physica B+C*, 1980, **99**, 81.

9 C. Delmas, J.-J. Braconnier, C. Fouassier and P. Hagenmuller, Electrochemical Intercalation of Sodium in Na$_x$CoO$_2$ Bronzes, *Solid State Ionics*, 1981, **3–4**, 165.

10 K. Kubota, S. Kumakura, Y. Yoda, K. Kuroki and S. Komaba, Electrochemistry and Solid-State Chemistry of NaMeO$_2$ (Me = 3d Transition Metals), *Adv. Energy Mater.*, 2018, **8**, 1703415.

11 P. F. Wang, Y. You, Y. X. Yin and Y. G. Guo, Layered Oxide Cathodes for Sodium-ion Batteries: Phase Transition, Air Stability, and Performance, *Adv. Energy Mater.*, 2018, **8**, 1701912.

12 X. Xiang, K. Zhang and J. Chen, Recent Advances and Prospects of Cathode Materials for Sodium-ion Batteries, *Adv. Mater.*, 2015, **27**, 5343.

13 Y. N. Zhou, P. F. Wang, X. D. Zhang, L. B. Huang, W. P. Wang, Y. X. Yin, S. Xu and Y. G. Guo, Air-stable and High-voltage Layered P3-type Cathode for Sodium-ion Full Battery, *ACS Appl. Mater. Interfaces*, 2019, **11**, 24184.

14 S. Guo, Y. Sun, J. Yi, K. Zhu, P. Liu, Y. Zhu, G. Z. Zhu, M. Chen, M. Ishida and H. Zhou, Understanding Sodium-ion Diffusion in Layered P2 and P3 Oxides via Experiments and First-principles Calculations: A Bridge between Crystal Structure and Electrochemical Performance, *NPG Asia Mater.*, 2016, **8**, e266.

15 P. Hou, M. Dong, Z. Lin, Z. Sun, M. Gong, F. Li and X. Xu, Alleviating the Jahn–Teller Distortion of P3-Type Manganese-Based Cathodes by Compositionally Graded Structure for Sodium-Ion Batteries, *ACS Sustain. Chem. Eng.*, 2023, **11**, 10785.

16 B. Song, E. Hu, J. Liu, Y. Zhang, X. Q. Yang, J. Nanda, A. Huq and K. Page, A Novel P3-type Na$_{2/3}$Mg$_{1/3}$Mn$_{2/3}$O$_2$ as High Capacity Sodium-Ion Cathode Using Reversible Oxygen Redox, *J. Mater. Chem. A*, 2019, **7**, 1491.

17 E. J. Kim, R. Tatara, T. Hosaka, K. Kubota, S. Kumakura and S. Komaba, Effects of Particle Size and Polytype on the Redox Reversibility of the Layered Na$_{0.76}$Ni$_{0.38}$Mn$_{0.62}$O$_2$ Electrode, *ACS Appl. Energy Mater.*, 2024, **7**, 1015.

18 K. Hashimoto, K. Ikeuchi, K. Kubota, T. Harada and S. Komaba, *The 82nd Annual Meeting of the Electrochemical Society of Japan*, Yokohama National University, Japan, 2015, p. 3J05.

19 K. Kubota, K. Hashimoto, Y. Yoda and S. Komaba, *3rd International Conference on Sodium Batteries, Geelong Waterfront*, Victoria, Australia, 2016, December 7–9.

20 K. Kubota, K. Hashimoto, Y. Yoda and S. Komaba, *11th Japan-France joint seminar on batteries*, Nantes, France, 2016, Septemper 20-22.

21 W. Hua, X. Yang, S. Wang, H. Li, A. Senyshyn, A. Tayal, V. Baran, Z. Chen, M. Avdeev, M. Knapp, H. Ehrenberg, I. Saadoune, S. Chou, S. Indris and X. Guo, Dynamic

5636 | *J. Mater. Chem. A*, 2026, **14**, 5626–5638

This journal is © The Royal Society of Chemistry 2026

inconsistency between electrochemical reaction and phase transition in Na-deficient layered cathode materials, *Energy Storage Mater.*, 2023, **61**, 102906.

22 X. Yang, S. Wang, H. Li, J. Tseng, Z. Wu, S. Indris, H. Ehrenberg, X. Guo and W. Hua, Unveiling the correlation between structural alterations and enhanced high-voltage cyclability in Na-deficient P3-type layered cathode materials via Li incorporation, *Electron*, 2024, **2**, e18.

23 J. Zhang, W. Wang, W. Wang, S. Wang and B. Li, Comprehensive Review of P2-Type $Na_{2/3}Ni_{1/3}Mn_{2/3}O_2$, a Potential Cathode for Practical Application of Na-Ion Batteries, *ACS Appl. Mater. Interfaces*, 2019, **11**, 22051.

24 Z. Lu, R. A. Donaberger and J. R. Dahn, Superlattice Ordering of Mn, Ni, and Co in Layered Alkali Transition Metal Oxides with P2, P3, and O3 Structures, *Chem. Mater.*, 2000, **12**, 3583.

25 S. Y. Lee, J. H. Kim and Y. C. Kang, Electrochemical Properties of P2-type $Na_{2/3}Ni_{1/3}Mn_{2/3}O_2$ Plates Synthesized by Spray Pyrolysis Process for Sodium-Ion Batteries, *Electrochim. Acta*, 2017, **225**, 86.

26 N. Yabuuchi, M. Kajiyama, J. Iwatate, H. Nishikawa, S. Hitomi, R. Okuyama, R. Usui, Y. Yamada and S. Komaba, P2-type $Na_x[Fe_{1/2}Mn_{1/2}]O_2$ Made from Earth-Abundant Elements for Rechargeable Na Batteries, *Nat. Mater.*, 2012, **11**, 512.

27 M. Li, D. L. Wood, Y. Bai, R. Essehli, M. R. Amin, C. Jafta, N. Muralidharan, J. Li and I. Belharouak, Eutectic Synthesis of the P2-Type $Na_xFe_{1/2}Mn_{1/2}O_2$ Cathode with Improved Cell Design for Sodium-Ion Batteries, *ACS Appl. Mater. Interfaces*, 2020, **12**, 23951.

28 J. Darga and A. Manthiram, Facile Synthesis of O3-Type $NaNi_{0.5}Mn_{0.5}O_2$ Single Crystals with Improved Performance in Sodium-Ion Batteries, *ACS Appl. Mater. Interfaces*, 2022, **14**, 52729.

29 M. Duffiet, D. Goonetilleke, F. Fauth, T. Brezesinski, J. Janek and M. Bianchini, Real-Time Crystallization of $LiCoO_2$ from β-$Co(OH)_2$ and Co_3O_4: Synthetic Pathways and Structural Evolution, *Chem. Mater.*, 2022, **34**, 9955.

30 B. Lin, Z. Wen, Z. Gu and S. Huang, Morphology and Electrochemical Performance of $Li[Ni_{1/3}Co_{1/3}Mn_{1/3}]O_2$ Cathode Material by a Slurry Spray Drying Method, *J. Power Sources*, 2008, **175**, 564.

31 G. D. Park and Y. C. Kang, Characteristics of Precursor Powders of a Nickel-Rich Cathode Material Prepared by A Spray Drying Process using Water-Soluble Metal Salts, *RSC Adv.*, 2014, **4**, 44203.

32 G. D. C. Csete de Györgyfalva and I. M. Reaney, Decomposition of $NiMn_2O_4$ Spinel: An NTC Thermistor Material, *J. Eur. Ceram. Soc.*, 2001, **21**, 2145.

33 J. Jung, J. Töpfer, J. Mürbe and A. Feltz, Microstructure and Phase Development in $NiMn_2O_4$ Spinel Ceramics during Isothermal Sintering, *J. Eur. Ceram. Soc.*, 1990, **6**, 351.

34 M. S. Islam and C. R. A. Catlow, Structural and Electronic Properties of $NiMn_2O_4$, *J. Phys. Chem. Solids*, 1988, **49**, 119.

35 T. Shahanas, G. Harichandran and B. Muthuraaman, Morphologically Tailored $NiMn_2O_4$ Nanocubic Material for High Energy-Power Density Asymmetric Supercapacitor

and Non-Enzymatic H_2O_2 Sensing, *Electrochim. Acta*, 2024, **493**, 144330.

36 Y. Koyama, T. Mizoguchi, H. Ikeno and I. Tanaka, Electronic Structure of Lithium Nickel Oxides by Electron Energy Loss Spectroscopy, *J. Phys. Chem. B*, 2005, **109**, 10749.

37 J. H. Seo, S. Na, S. J. Ahn, K. Park, S. Lee, J. Lee and J. H. Kwon, Electron Beam-Induced Effects on a Ni-Rich Layered Cathode Material: A Comprehensive Investigation Using STEM and EELS, *J. Phys. Chem. C*, 2024, **128**, 9099.

38 T. C. Rojas, M. Âa, J. S. Âs, A. Caballero, Y. Koltypin, A. Gedanken, L. Ponsonnet, B. Vacher, J. M. Martin, A. Ân and F. Ândez, TEM, EELS and EFTEM Characterization of Nickel Nanoparticles Encapsulated in Carbon, *J. Mater. Chem.*, 2000, **10**, 715.

39 H. Yu, G. Qin, J. Wang, X. Zhao, L. Li, X. Yu, X. Zhang, Z. Lu and X. Yang, Improving Oxygen Reduction Reaction Performance via Central Ions Enhanced Crystal-Field Splitting of MnO_6 Octahedron, *ACS Catal.*, 2022, **12**, 12890.

40 A. Prodi, E. Gilioli, A. Gauzzi, F. Licci, M. Marezio, F. Bolzoni, Q. Huang, A. Santoro and J. W. Lynn, Charge, Orbital and Spin Ordering Phenomena in the Mixed Valence Manganite $(NaMn^{3+}_3)(Mn^{3+}_2Mn^{4+}_2)O_{12}$, *Nat. Mater.*, 2004, **3**, 48.

41 J. Deng, W. Bin Luo, S. L. Chou, H. K. Liu and S. X. Dou, Sodium-Ion Batteries: From Academic Research to Practical Commercialization, *Adv. Energy Mater.*, 2018, **8**, 1701428.

42 E. Goikolea, V. Palomares, S. Wang, I. R. de Larramendi, X. Guo, G. Wang and T. Rojo, Na-Ion Batteries—Approaching Old and New Challenges, *Adv. Energy Mater.*, 2020, **10**, 2002055.

43 Z. Lu, Z. Chen and J. R. Dahn, Lack of Cation Clustering in Li$[Ni_xLi_{1/3-2x/3}Mn_{2/3-x/3}]O_2$ ($0 < x \leq 1/2$) and Li$[Cr_xLi_{(1-x)/3}Mn_{(2-2x)/3}]O_2$ ($0 < x < 1$), *Chem. Mater.*, 2003, **15**, 3214.

44 Z. Lu and J. R. Dahn, Intercalation of Water in P2, T2 and O2 Structure $A_z[Co_xNi_{1/3-x}Mn_{2/3}]O_2$, *Chem. Mater.*, 2001, **13**, 1252.

45 F. Frati, M. O. J. Y. Hunault and F. M. F. De Groot, Oxygen K-edge X-ray Absorption Spectra, *Chem. Rev.*, 2020, **120**, 4056.

46 C. Lin, X. Meng, M. Liang, W. Li, J. Liang, T. Liu, X. Ke, J. Liu, Z. Shi and L. Liu, Facilitating Reversible Transition Metal Migration and Expediting Ion Diffusivity via Oxygen Vacancies for High Performance O3-Type Sodium Layered Oxide Cathodes, *J. Mater. Chem. A*, 2022, **11**, 68.

47 S. T. Myung, K. Hosoya, S. Komaba, H. Yashiro, Y. K. Sun and N. Kumagai, Improvement of Cycling Performance of $Li_{1.1}Mn_{1.9}O_4$ at 60°C by NiO Addition for Li-Ion Secondary Batteries, *Electrochim. Acta*, 2006, **51**, 5912.

48 Y. Liu, J. Liao, Z. Tang, Y. Chao, W. Chen, X. Wu and W. Wu, Improved Sodium Storage Performance of Zn-Substituted P3-$Na_{0.67}Ni_{0.33}Mn_{0.67}O_2$ Cathode Materials for Sodium-Ion Batteries, *J. Electron. Mater.*, 2023, **52**, 864.

49 S. Maddukuri, P. Valerie and V. V. Upadhyayula, Synthesis and Electrochemical Study of New P3 Type Layered $Na_{0.6}Ni_{0.25}Mn_{0.5}Co_{0.25}O_2$ for Sodium-Ion Batteries, *ChemistrySelect*, 2017, **2**, 5660.

This journal is © The Royal Society of Chemistry 2026

J. Mater. Chem. A, 2026, **14**, 5626–5638 | **5637**

50 L. G. Chagas, D. Buchholz, C. Vaalma, L. Wuab and S. Passerini, P-type $Na_xNi_{0.22}Co_{0.11}Mn_{0.66}O_2$ Materials: Linking Synthesis with Structure and Electrochemical Performance, *J. Mater. Chem. A*, 2014, **2**, 20263.

51 S. Saxena, M. Badole, H. N. Vasavan, V. Srihari, A. K. Das, P. Gami, N. Dagar, S. Deswal, P. Kumar, H. K. Poswal and S. Kumar, Elucidating the Electrochemical Behavior of a P3-type High-Na-Content Cathode, *Energy Fuels*, 2024, **38**, 12140.

52 S. Zhao, X. Yu and Y. Zhao, A Water-Stable High-Voltage P3-Type Cathode for Sodium-Ion Batteries, *Chin. Chem. Lett.*, 2024, **35**, 109933.

53 L. Yu, H. Dong, Y. X. Chang, Z. Cheng, K. Xu, Y. H. Feng, D. Si, X. Zhu, M. Liu, B. Xiao, P. F. Wang and S. Xu, Elucidation of the Sodium Kinetics in Layered P-Type Oxide Cathodes, *Sci. China: Chem.*, 2022, **65**, 2005.

54 L. Zhang, J. Wang, G. Schuck, F. Xi, L. Du, M. Winter, G. Schumacher and J. Li, Stabilizing P3-type Oxides as Cathodes for High-Rate and Long-Life Sodium Ion Batteries by Disordered Distribution of Transition Metals, *Small Methods*, 2020, **4**, 2000422.

5638 | *J. Mater. Chem. A*, 2026, **14**, 5626–5638

This journal is © The Royal Society of Chemistry 2026